Strategies to maximize the performance of a STED microscope

Silvia Galiani,[1] Benjamin Harke,[1] Giuseppe Vicidomini,[1] Gabriele Lignani,[2] Fabio Benfenati,[2] Alberto Diaspro,[1] and Paolo Bianchini[1,*]

[1]*Nanophysics, Istituto Italiano di Tecnologia, Genoa, Italy*
[2]*Neuroscience and Brain Technologies, Istituto Italiano di Tecnologia, Genoa, Italy*
[*] *paolo.bianchini@iit.it*

Abstract: In stimulated emission depletion (STED) microscopy, the spatial resolution scales as the inverse square root of the STED beam's intensity. However, to fully exploit the maximum effective resolution achievable for a given STED beam's intensity, several experimental precautions have to be considered. We focus our attention on the temporal alignment between the excitation and STED pulses and the polarization state of the STED beam. We present a simple theoretical framework that help to explain their influence on the performance of a STED microscope and we validate the results by imaging calibration and biological samples with a custom made STED architecture based on a supercontinuum laser source. We also highlight the advantages of using time gating detection in terms of temporal alignment.

OCIS codes: (350.5730) Resolution; (180.2520) Fluorescence microscopy; (000.2170) Equipment and techniques.

References and links

1. A. Diaspro, *Confocal and Two-Photon Microscopy* (Wiley-Liss, 2002).
2. E. Abbe, "Beitrage zur theorie des mikroskops und der mikroskopischen wahrnehmung," Arch. Mikrosk. Anat. **9**(1), 413–418 (1873).
3. B. Huang, H. Babcock, and X. Zhuang, "Breaking the diffraction barrier: super-resolution imaging of cells," Cell **143**(7), 1047–1058 (2010).
4. S. W. Hell, "Microscopy and its focal switch," Nat. Methods **6**(1), 24–32 (2009).
5. A. Diaspro, *Nanoscopy and multidimensional optical fluorescence microscopy* (Chapman and Hall/CRC, 2010).
6. S. W. Hell, "Far-field optical nanoscopy," Science **316**(5828), 1153–1158 (2007).
7. V. Westphal, S. O. Rizzoli, M. A. Lauterbach, D. Kamin, R. Jahn, and S. W. Hell, "Video-rate far-field optical nanoscopy dissects synaptic vesicle movement," Science **320**(5873), 246–249 (2008).
8. C. Eggeling, C. Ringemann, R. Medda, G. Schwarzmann, K. Sandhoff, S. Polyakova, V. N. Belov, B. Hein, C. von Middendorff, A. Schönle, and S. W. Hell, "Direct observation of the nanoscale dynamics of membrane lipids in a living cell," Nature **457**(7233), 1159–1162 (2009).
9. B. Harke, C. K. Ullal, J. Keller, and S. W. Hell, "Three-dimensional nanoscopy of colloidal crystals," Nano Lett. **8**(5), 1309–1313 (2008).
10. R. Schmidt, C. A. Wurm, S. Jakobs, J. Engelhardt, A. Egner, and S. W. Hell, "Spherical nanosized focal spot unravels the interior of cells," Nat. Methods **5**(6), 539–544 (2008).
11. G. Moneron and S. W. Hell, "Two-photon excitation STED microscopy," Opt. Express **17**(17), 14567–14573 (2009).
12. J. B. Ding, K. T. Takasaki, and B. L. Sabatini, "Supraresolution imaging in brain slices using stimulated-emission depletion two-photon laser scanning microscopy," Neuron **63**(4), 429–437 (2009).
13. F. M. Wurm, K. A. Gwinn, and R. E. Kingston, "Inducible overproduction of the mouse c-myc protein in mammalian cells," Proc. Natl. Acad. Sci. U.S.A. **83**(15), 5414–5418 (1986).
14. S. W. Hell, "Far-field optical nanoscopy," in *Single Molecule Spectroscopy in Chemistry, Physics and Biology,* R. R. A. Graslund and J. Widengren, eds. (Springer, 2010), pp. 365–398.
15. G. Donnert, J. Keller, R. Medda, M. A. Andrei, S. O. Rizzoli, R. Lührmann, R. Jahn, C. Eggeling, and S. W. Hell, "Macromolecular-scale resolution in biological fluorescence microscopy," Proc. Natl. Acad. Sci. U.S.A. **103**(31), 11440–11445 (2006).
16. M. Leutenegger, C. Eggeling, and S. W. Hell, "Analytical description of STED microscopy performance," Opt. Express **18**(25), 26417–26429 (2010).

#161451 - $15.00 USD Received 13 Jan 2012; revised 26 Feb 2012; accepted 1 Mar 2012; published 15 Mar 2012

17. K. I. Willig, B. Harke, R. Medda, and S. W. Hell, "STED microscopy with continuous wave beams," Nat. Methods **4**(11), 915–918 (2007).
18. B. R. Rankin and S. W. Hell, "STED microscopy with a MHz pulsed stimulated-Raman-scattering source," Opt. Express **17**(18), 15679–15684 (2009).
19. D. Wildanger, E. Rittweger, L. Kastrup, and S. W. Hell, "STED microscopy with a supercontinuum laser source," Opt. Express **16**(13), 9614–9621 (2008).
20. J. Bückers, D. Wildanger, G. Vicidomini, L. Kastrup, and S. W. Hell, "Simultaneous multi-lifetime multi-color STED imaging for colocalization analyses," Opt. Express **19**(4), 3130–3143 (2011).
21. D. Wildanger, R. Medda, L. Kastrup, and S. W. Hell, "A compact STED microscope providing 3D nanoscale resolution," J. Microsc. **236**(1), 35–43 (2009).
22. J. R. Moffitt, C. Osseforth, and J. Michaelis, "Time-gating improves the spatial resolution of STED microscopy," Opt. Express **19**(5), 4242–4254 (2011).
23. G. Vicidomini, G. Moneron, K. Y. Han, V. Westphal, H. Ta, M. Reuss, J. Engelhardt, C. Eggeling, and S. W. Hell, "Sharper low-power STED nanoscopy by time gating," Nat. Methods **8**(7), 571–573 (2011).
24. M. Dyba and S. W. Hell, "Photostability of a fluorescent marker under pulsed excited-state depletion through stimulated emission," Appl. Opt. **42**(25), 5123–5129 (2003).
25. C.-K. Chou, W.-L. Chen, P. T. Fwu, S.-J. Lin, H.-S. Lee, and C.-Y. Dong, "Polarization ellipticity compensation in polarization second-harmonic generation microscopy without specimen rotation," J. Biomed. Opt. **13**(1), 014005 (2008).
26. B. Harke, J. Keller, C. K. Ullal, V. Westphal, A. Schönle, and S. W. Hell, "Resolution scaling in STED microscopy," Opt. Express **16**(6), 4154–4162 (2008).
27. E. Auksorius, B. R. Boruah, C. Dunsby, P. M. P. Lanigan, G. Kennedy, M. A. A. Neil, and P. M. W. French, "Stimulated emission depletion microscopy with a supercontinuum source and fluorescence lifetime imaging," Opt. Lett. **33**(2), 113–115 (2008).
28. X. Hao, C. Kuang, T. Wang, and X. Liu, "Effects of polarization of the de-excitation dark focal spot in STED microscopy," J. Opt. **12**(11), 115707 (2010).
29. P. Dedecker, B. Muls, J. Hofkens, J. Enderlein, and J.-I. Hotta, "Orientational effects in the excitation and de-excitation of single molecules interacting with donut-mode laser beams," Opt. Express **15**(6), 3372–3383 (2007).
30. S. W. Hell and A. Schonle, "Nanoscale resolution in far-field fluorescence microscopy," in *Science of Microscopy II*, P. W. Hawkes and J. C. H. Spence, eds. (Springer, 2007), pp. 790–834.
31. S. Deng, L. Liu, Y. Cheng, R. Li, and Z. Xu, "Effects of primary aberrations on the fluorescence depletion patterns of STED microscopy," Opt. Express **18**(2), 1657–1666 (2010).
32. J. Keller, A. Schönle, and S. W. Hell, "Efficient fluorescence inhibition patterns for RESOLFT microscopy," Opt. Express **15**(6), 3361–3371 (2007).
33. L. Qu, Y. Akbergenova, Y. Hu, and T. Schikorski, "Synapse-to-synapse variation in mean synaptic vesicle size and its relationship with synaptic morphology and function," J. Comp. Neurol. **514**(4), 343–352 (2009).
34. G. Vicidomini, P. Boccacci, A. Diaspro, and M. Bertero, "Application of the split-gradient method to 3D image deconvolution in fluorescence microscopy," J. Microsc. **234**(1), 47–61 (2009).
35. B. R. Rankin, R. R. Kellner, and S. W. Hell, "Stimulated-emission-depletion microscopy with a multicolor stimulated-Raman-scattering light source," Opt. Lett. **33**(21), 2491–2493 (2008).

1. Introduction

Far-field fluorescence microscopy is widely used in life-science due to a number of rather exclusive advantages [1] such as the non-invasive access to the interior of the (living) cells, the specific and sensitive detection of cellular constituents and the simple sample preparation. However, many cellular constituents are too small to be resolved with standard far-field fluorescence microscopy whose spatial resolution is restricted by diffraction to several hundreds of nanometers [2]. Over the last years, several concepts for overcoming the diffraction barrier and preserving the advantages of far-field fluorescence microscopy have been developed [3–5]. While they all rely on the modulation of the fluorescence emission such that adjacent features fluoresce sequentially in time, these techniques (usually referred as far-field optical nanoscopy techniques) differ from each other for the mechanisms and/or methods used to modulate the fluorescence [6].

Among the reported methods, stimulated emission depletion (STED) microscopy stands out by its ability to instantly provide signal from selected nanosized volume in the sample, which makes it particularly suited for fast imaging [7] and spectroscopy [8] at molecular scale.

In most STED microscopes, a laser beam inducing stimulated emission, the so called STED beam, is spatially overlaid with a regular excitation beam. The STED beam produces a doughnut-shaped focal pattern featuring a "zero"-intensity point in its center, thus, inhibits

#161451 - $15.00 USD Received 13 Jan 2012; revised 26 Feb 2012; accepted 1 Mar 2012; published 15 Mar 2012

fluorescence emission everywhere but at the center of the focus. When the intensity of the STED beam at the doughnut crest saturates the stimulated emission transition, the effective fluorescence volume is confined to subdiffraction size along the lateral direction, while keeping the size in the axial direction untouched. Scanning the co-aligned beams through the sample, or vice versa, yields to images whose lateral resolution is tuned by the intensity of the STED light. For a substantial improvement of resolution along all spatial directions more complex instrumentation is needed. Two powerful approaches were shown so far. The former uses two different beams, simultaneously combined with two different phase plates: one improving the lateral and the other one the axial resolution [9]. The latter uses a 4pi-like configuration to generate a STED focal pattern that leads to an isotropic resolution improvement [10]. A further concept that helps three-dimensional imaging especially in deep scattering samples, but does not lead to an axial resolution enhancement *per se*, is the combination of STED with two-photon-excitation [11, 12]. Despite STED has been successfully extended to improve also the axial dimension, one has to keep in mind that many applications require just a lateral resolution improvement since the observation volume is already confined along the optical axis. This is particularly the case for imaging that can be carried out on a coverslip surface [13].

Since most of the dyes exhibit excited-state lifetimes in the 1-10 ns range and a stimulated emission cross section (σ_{STED}) of ~10^{-16} cm^2, focal STED intensity (I_{STED}) of 0.1-1 $GWcm^{-2}$ is necessary to effectively saturate the stimulated emission transition and thereby achieve subdiffraction confinements of the effective fluorescence volume [14]. Driven by this demand of high STED intensity but low average power, STED microscopy has been initially implemented with (ultra) short pulsed mode-locked laser systems. In pulsed STED implementation, the pulses of the STED beam reaches the focal plane immediately after the excitation pulses so as to instantly de-excite potentially excited molecules. The complexity of the system increases when implementing STED microscopy for dyes in the visible range, since the mode-locked laser has to be coupled to an optical parametric oscillator (OPO). Moreover, efficient nonlinear wavelength conversion requires the pump and hence the OPO to deliver pulses of 200–300 fs duration [15]. This is a drawback since STED is most effective with 0.1–2 ns pulses [16]. Thereby the pulses have to be stretched by dispersion using gratings or fibers, which add further complexity to the system. Such a pulse elaboration contributed to the notion that STED microscopy is inherently expensive and requires complex instrumentation as well as diligent operation and maintenance. The wider use of STED microscopy has been encouraged by the introduction of simplified and more economic STED microscope implementations, which relies on CW laser sources [17], stimulated-Raman-scattering sources [18] or supercontinuum (SC) laser sources [19]. The latter solution is particularly appealing, since it uses the same laser source for both excitation and STED beam. Moreover, it can be easily extended to multi-color imaging [20]. However, while the use of a supercontinuum laser has increased the acceptance of STED microscopy, the implementation of such a solution requires several experimental strategies in order to achieve the maximum resolution. In particular, excitation and STED beams still require alignment in all spatial directions as well as in temporal dimension. Moreover a good quality of the “zero”-intensity point of the doughnut-shaped STED focus is mandatory.

In this paper, we report on a theoretical and experimental study focusing on the performance of a SC STED microscope in dependence on the time-alignment between excitation and STED pulses as well as the influence of the polarization of the STED beam to the quality of the “zero”-intensity point. Finally, we will show that, when the signal-to-noise ratio (SNR) is not a limitation, a delay of the STED pulse arrivals, relative to the excitation pulse, can be compensated by applying time-gated detection [22, 23].

#161451 - $15.00 USD Received 13 Jan 2012; revised 26 Feb 2012; accepted 1 Mar 2012; published 15 Mar 2012

2. Materials and methods

2.1 STED setup

Our STED microscope (Fig. 1) employs a commercial supercontinuum fiber laser at 2 MHz (SC-450-PP-HE, Fianium, Southampton, UK) providing both the excitation and the STED pulses. In order to separate the excitation beam from the STED beam a proper dichroic mirror (FF-585DI01, Semrock, New York, USA) divides the laser output into two parts. Successively, the two beams pass through different color filters (FF01-571/15-25, for excitation and FF01-720/13 for STED, Semrock) in order to select the appropriate wavelengths for the excitation and the STED beams.

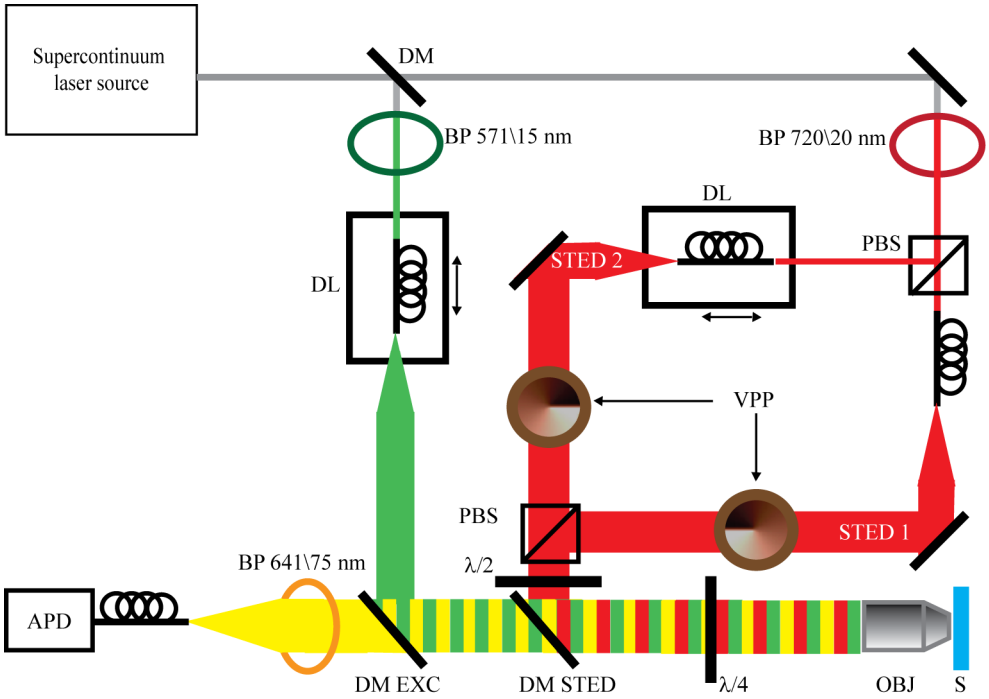

Fig. 1. Scheme of the STED architecture realized. BP: bandpass filter, DL: delay line, PBS: polarizing beam splitter, VPP: vortex phase plate, DM: dichroic mirror, OBJ: objective lens, S: sample, APD: avalanche photodiode.

Since a defined polarization state has to be used in the depletion pattern of the STED beam, the originally unpolarized STED beam is further split into two beams by a polarizing beam splitter cube (B. Halle GmbH, Berlin, Germany) orthogonal polarized. Each of the three beams is coupled into a polarization maintaining single mode optical fiber (P1- 88PM-FC-2, Thorlabs GmbH Europe, Dachau, Germany, for excitation and PMC-780-4,8-NA013-3-opc-50-P, Schäfter + Kirchhoff GmbH, Hamburg, Germany, for STED). Each collimator is mounted on an optical rail. Since we use the very same light source to generate the three beams, they are synchronized by design and their arrival at the focal plane can be controlled by using the optical rail to change the three optical path lengths. It is also important to observe that the ~80 ps pulses generated by the laser source are already appropriated for STED and do not require any further stretching [24]. At the fibers outputs, the three beams are separately collimated (60FC-0-M60-54, Schäfter + Kirchhoff GmbH for excitation and (60FC-0-M40-10, Schäfter + Kirchhoff GmbH for STED). The two STED beams pass through two vortex phase plates (RPC Photonics, Rochester, NY, USA) before they are recombined by another polarizing beam splitter cube. Notably, the two phase plates feature different orientations of

#161451 - $15.00 USD Received 13 Jan 2012; revised 26 Feb 2012; accepted 1 Mar 2012; published 15 Mar 2012

the vortex in order to match the orthogonal polarization of the two STED beams. The excitation beam and the STED beams are coupled into an oil immersion objective lens (HCX PL APO 100 × /1.4 Oil STED orange, Leica Microsystems, Wetzlar, Germany) by two dichroic mirrors (FF585-DI01 for excitation, FF670-DI01 for STED, Semrock). A half waveplate is inserted before the dichroic mirror in order to precompensate for the alterations of the polarization-states induced mainly by the dichroic [25]. The half waveplate, in combination with the quarter waveplate inserted before the objective lens, allows obtaining a precise circular polarization of the STED beams at the back aperture of the objective. Now assuming that the objective lens does not alter significantly the polarization state, the two generated STED foci are of circular polarization with contradicting sense of rotation. Polarization measurements at the back aperture of the objective are done by a polarization analyzer device (Schäfter + Kirchhoff GmbH). Fluorescence is collected by the same objective lens, filtered out by the two dichroic mirrors and a band pass filter (FF01-641/75-25, Semrock) and then focused into a multimode optical fiber (M31L01, Thorlabs GmbH Europe), which serves as confocal pinhole. An avalanche photodiode module (SPCM-AQRH-13-FC, Perkin Elmer, Vaudreuil, Québec, Canada), connected to a time correlated single photon counting board (SPC-830, Becker & Hickl GmbH, Berlin, Germany), record the signal. The scanning of the sample is realized by a fine xyz piezo stage (P- 17-3CD Physik Instrumente GmbH, Karlsruhe, Germany). Power values reported in this work are measured at the back focal plane of the objective lens. All acquisition operations are software controlled by Imspector (Max-Planck-Innovations, Germany).

2.2 Sample preparation

Beads sample: Fluorescent microspheres (FluoSpheres, red fluorescent (580/605), diameter 0.04 µm, Invitrogen, USA), are diluted in Milli-Q-water with a dilution factor $1:10^4$. A drop of diluted beads is attached to the coverslip using poly-L-lysine (Sigma Aldrich) and then the coverslip is mounted on a microscope slide and embedded in the mounting medium Mowiol (Sigma-Aldrich, Europe).

Biological sample: Primary hippocampal neurons are prepared from C57BL/6J mouse embryos in accordance with the guidelines established by the European Community Council (Directive of November 24th, 1986) and approved by the National Council on Animal Care of the Ministry of Health. Dissociated neurons are plated at low density (20 cells/mm^2) and maintained in a culture medium consisting of Neurobasal, B-27 (1:50 v/v), glutamax (1% w/v), penicillin-streptomycin (1%) in 5% CO_2. Neurons are fixed at 14 days in vitro (DIV) with 4% paraformaldehyde in 0.1 M Phosphate buffer, rinsed several times in PBS, incubated 10 minutes in 50 mM NH_4Cl, blocked and permeabilized in 0.1% Saponin/3% BSA in PBS for 1 hour. Samples are incubated with primary rabbit antibodies directed to the vesicular GABA transporter VGAT (Synaptic System, cat # 131 011, 1:500) diluited 1:500 in blocking buffer for 2 hours at room temperature. Coverslips are washed twice in 0.1% saponin in PBS, and once in blocking buffer for 10 minutes and then incubated for 1 hour with goat anti-rabbit ATTO590 antibodies (Sigma-Aldrich S.r.l., Milan, Italy) diluted 1:500 in blocking buffer. Samples are washed twice in 0.1% saponin in PBS and twice in PBS for 5 minutes each and mounted on a drop of Immumount (ThermoScientific, Erembodegem, Belgium).

3. High-resolution alignment prerequisites

3.1 Time-delays between excitation and STED pulses

It is worth noting that in STED microscopy, the spatial resolution is determined by the ability of the depletion beam to inhibit fluorescence emission from potentially excited fluorophores. The higher the probability to inhibit the fluorescence by stimulated emission, the higher is the final spatial confinement of the effective fluorescent volume. In the case of pulsed STED implementation the probability η of spontaneous emission of an excited fluorophore depends

#161451 - $15.00 USD Received 13 Jan 2012; revised 26 Feb 2012; accepted 1 Mar 2012; published 15 Mar 2012

on the intensity of the STED beam I_{STED}, and decreases in first approximation as $\eta(I_{STED})$ ~$\exp(-I_{STED}T_{STED}\sigma_{STED})$, where T_{STED} is the duration of the STED pulse and σ_{STED} is the stimulated emission cross-section [15]. Hence, a doughnut shaped focal distribution of the STED intensity $I_{STED}(r)$ featuring $I^{m}_{STED} = \max(I_{STED}(r))$ at the doughnut crest and $I_{STED}(r = 0) = 0$ at the center quenches the fluorescence signal throughout the focal region, except at the doughnut center. The resulting full-width at half-maximum (FWHM) of the effective fluorescent area follows $d \sim d_c/\sqrt{(1 + I^{m}_{STED}\, T_{STED}\sigma_{STED})}$, where d_c represents the FWHM of the point-spread-function (PSF) of the corresponding confocal system [26].

However, this first approximation assumes a perfect time-sequence of the experiment, namely, excitation, stimulated emission and fluorescence detection act all sequentially and continuously in time without overlap. Briefly, the excitation pulse prepares the fluorophores in the excited state, then the stimulated emission pulse inhibits the fluorophores and finally the detection system collects the fluorescence signal. In such a way, early spontaneous emission, which occurs in the focal periphery during the excitation and depletion processes, is discarded [23, 27]. In most of the cases, in particular when the excited state lifetime of the fluorophore is much longer than the pulse width of the STED and excitation beam, such early spontaneous emission is negligible. Thereby, by providing proper time-alignment between the excitation and the STED beams, the fluorescence signal can be collected during all the measurement and a time-gated detection is not strictly necessary. On the other hand, if the depletion beam is delayed with respect to the excitation beam, early spontaneous emission cannot be ignored and a time-gated detection can be applied in order to block the early emitted photons.

The presence of early emission due to late depletion, as well as, the fluorescence signal generated by the STED beam itself, can be seen as an incomplete depletion process. Such incomplete depletion process can be modeled by adding a constant offset δ in the spontaneous emission probability (or remaining fluorescence) η (Fig. 2(a) inset), i.e. $\eta(I_{STED}) = (1-\delta) \times exp(-I_{STED}T_{STED}\sigma_{STED}) + \delta$.

To demonstrate the influence of the incomplete fluorescence quenching, we derive an analytical approximation of the effective-PSF h_{eff} of the STED microscope. Hence, at low (far from saturation) excitation intensity, h_{eff} of a STED microscope is given by the probability of spontaneous emission multiplied with the PSF of a confocal system, $h_{eff}(r) = h_{conf}(r) \times \eta(I_{STED}(r))$. In the neighborhood of its center, the confocal PSF can be well described by a Gaussian distribution, $h_{conf}(r) = exp(-4ln(2)r^2/d_c)$ and the doughnut STED intensity pattern by a sinusoidal standing wave distribution, $I_{STED}(r) = sin^2(r\pi/p_d)$, where p_d is the peak-to-peak distance of the doughnut crests. For an increasing offset δ, h_{eff} shows a strong pedestal due to incomplete inhibition of the fluorescence signal. Figure 2(a) shows the effective PSF for values of δ chosen between 0 and 0.2. This is within possible experimental conditions considering time alignment variations and fluorescence excitation due to the STED beam. The imaging performance with such a kind of effective PSF will not result in a reduced resolution, but in a significant decrease in the imaging contrast. For δ ~0.2 high resolution imaging would still be possible, but only in case the structure of interest is sparse enough so that the contribution of adjacent objects to the total signal is low.

#161451 - $15.00 USD Received 13 Jan 2012; revised 26 Feb 2012; accepted 1 Mar 2012; published 15 Mar 2012

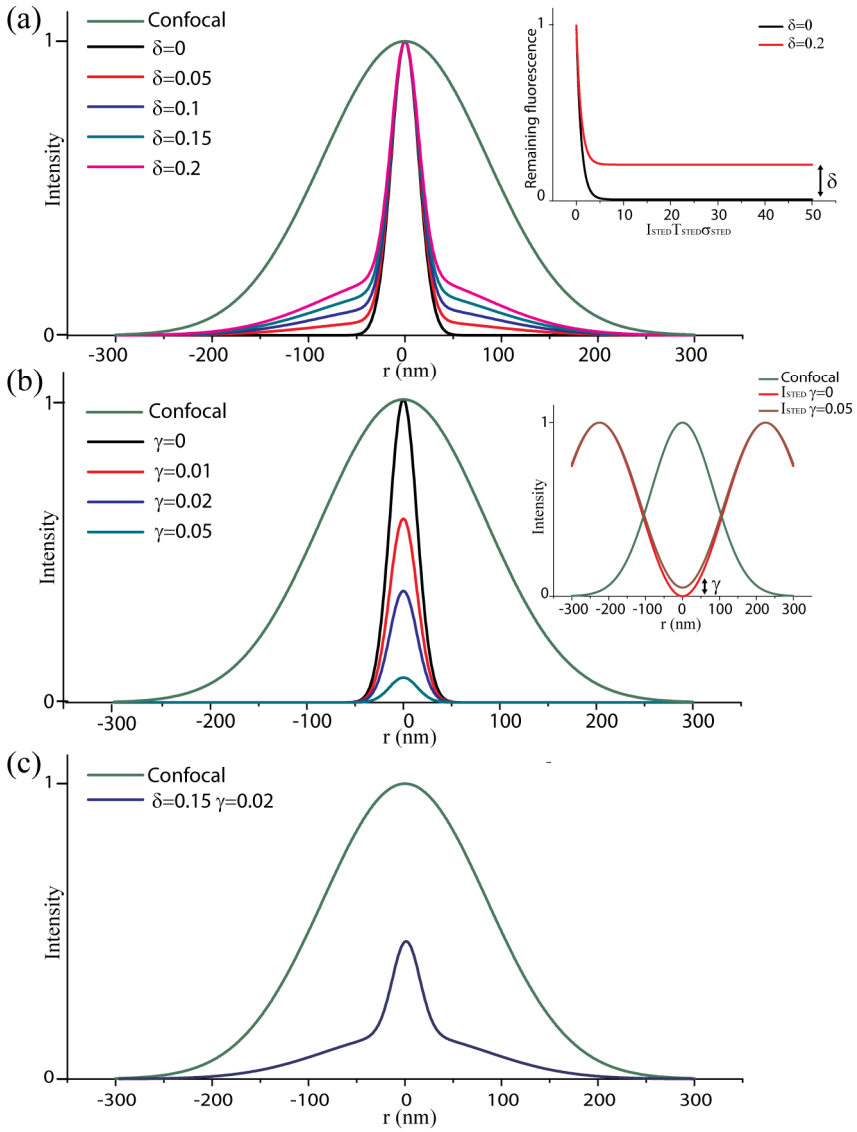

Fig. 2. Calculated STED effective PSF for different incomplete inhibition factor δ (a), imperfections of the "zero"-intensity γ (b) and their combinations (c). Inset (a): fluorescence inhibition as function of the STED energy. Inset (b): radial distributions of intensity at the focus of the doughnut shape STED beam and Gaussian confocal beam. Calculations with d_c = 200 nm, p_d = 400 nm and $I^m_{STED}T_{STED}\sigma_{STED}$ = 50.

Importantly, in case δ stems mainly from delayed STED pulse arrival the pedestal of the effective PSF can be removed by using time-gated detection, i.e. collecting photons after the action of the STED beam is completed [22, 23]. Thereby unwanted photons generated at the periphery of the doughnut center are discarded. However, time gating also rejects 'desired' photons, namely those that are emitted in the doughnut center. Therefore, the removal of the pedestal and the consequent image contrast increase has to be pondered against the reduction of the overall signal.

#161451 - $15.00 USD Received 13 Jan 2012; revised 26 Feb 2012; accepted 1 Mar 2012; published 15 Mar 2012

3.2 Polarization state of the STED beams

Now, apart from the incomplete fluorescence depletion, a further experimental critical condition originates from the imperfections of the "zero"-intensity point of the doughnut-shaped focal intensity distribution of the STED beam. In fact, a residual intensity γ in the center of the doughnut, related to the doughnut crest (Fig. 2(b) inset), i.e. $I_{\mathrm{STED}}(r) = I^{m}_{STED} \times ((1-\gamma) \times sin^2(r\pi/ p_d) + \gamma)$, results in a fluorescence quenching also in the central position of the doughnut and thereby in a reduction of the peak value of the effective PSF with respect to the corresponding confocal PSF (Fig. 2(b)). Once the standard experimental requirements in terms of surface flatness of the optical components used (typically $\lambda/10$ surface flatness is requested) are fulfilled an imperfect "zero"-intensity point stems mainly from an inappropriate polarization state. It has been theoretically demonstrated that when using a vortex phase plate the circular polarization of the STED beams is crucial to obtain a high quality "zero"-intensity point [28]. In a nutshell, circular polarization of the STED beam causes all vectorial components of the light field to interfere destructively at the geometric focal point, thus creating a deep doughnut minimum in case the sense of rotation of the polarization corresponds to the slope of the vortex phase pattern. Notably, circular polarization of the STED beam minimizes also photoselection effects that can reduce the effective cross-section of the stimulated depletion process and thereby reduce the strength of the inhibition process [29].

In practice, values for $\gamma < 0.01$ can be obtained under the best polarization alignment conditions [26]. In cases for $\gamma > 0.01$ the reduction of brightness could be compensated by increasing the pixel dwell-time. Unfortunately the photostability of the fluorescent marker as well as the desired image acquisition speed impose an experimental limit. As a consequence, the signal-to-noise and signal-to-background ratio of the image drastically deteriorates. Moreover, such imperfection on the "zero" turned out to have also a strong impact on the resolution performance [16, 30].

Figure 2(b) shows the effective PSF for $\gamma = 0$, 0.01, 0.02, 0.05 and the strong influence to the effective PSF is straight visible: already for $\gamma = 0.02$ the resulting peak intensity shrinks down to well below 50% of the original value. The final value for the peak reduction depends on the factor $I^{\mathrm{m}}_{\mathrm{STED}} T_{\mathrm{STED}} \sigma_{\mathrm{STED}}$ representing the level of saturation in the doughnut area, thus directly influencing the final resolution of the STED microscope. For all the simulations in Fig. 2 this factor was set to 50 that is a typical saturation level in a high resolution STED microscope [26].

The parameters δ and γ are independent from each other, and therefore any combination of these values can occur in the final experiment. Figure 2(c) shows the normalized effective PSF for $\gamma = 0.05$ and $\delta = 0.2$. It turns out that the pedestal of the PSF shape is further enhanced relative to the peak of the PSF. Such a PSF leads to a significant decrease of the image quality since the effective resolution strongly suffers from a poor signal-to-noise ratio.

In case the experimental parameters δ and γ are not properly optimized, these simple simulations show the relevant influence on the final performance of a STED microscope. Following such an analysis, in the next paragraph we provide the experimental evidence of δ and γ optimization obtained with our SC-STED architecture.

4. Results

4.1 Time-delays between excitation and STED pulses

In the previous paragraph the influence of a residual fluorescence signal δ to the final shape of the PSF has been discussed. As mentioned before, the reason for a remaining fluorescence after the STED pulse can be various, but surely in pulsed STED systems the temporal alignment of the excitation pulse relative to the STED pulse will have a direct influence on γ and therefore we will focus our attention to the temporal beam alignment in this section.

#161451 - $15.00 USD Received 13 Jan 2012; revised 26 Feb 2012; accepted 1 Mar 2012; published 15 Mar 2012

A readily implementable method for the time-alignment of the three beams uses the residual fluorescence signal generated by a uniform constantly emitting sample as figure of merit: we spatially co-aligned the STED and the excitation beams (all Gaussian shaped without using the vortex phase pattern in the STED beam paths) and we focused the beams into an aqueous solution of the fluorophore ATTO594. Firstly, we considered the temporal alignment of the excitation beam relative to the first STED beam (STED1). Transiently switching on and off STED1, we measured the relative residual of fluorescence as function of the time position of the excitation pulse (by varying the delay line of the excitation beam). Now, the time position that minimizes the relative residual fluorescence corresponds to the best time position for the excitation beam (Fig. 3(a)). We fixed the delay line for the excitation beam at the best time position and repeated the same procedure for the second STED beam (by varying the delay line of the second STED beam, STED2). The time position that minimizes the relative residual fluorescence corresponds to the best time position for the second STED beam (Fig. 3(b)). At the end of these steps, the efficiency to quench the fluorescence is maximized with respect to the time sequence of the three beams.

Unless time-gated detection is, in most cases, not mandatory for pulsed STED implementation, it helps to relax the constraints on the time-alignment of the beams and thereby to simplify the time alignment procedure. By keeping the time position of the two STED beams fixed, we changed the time position of the excitation pulses (Fig. 3c).

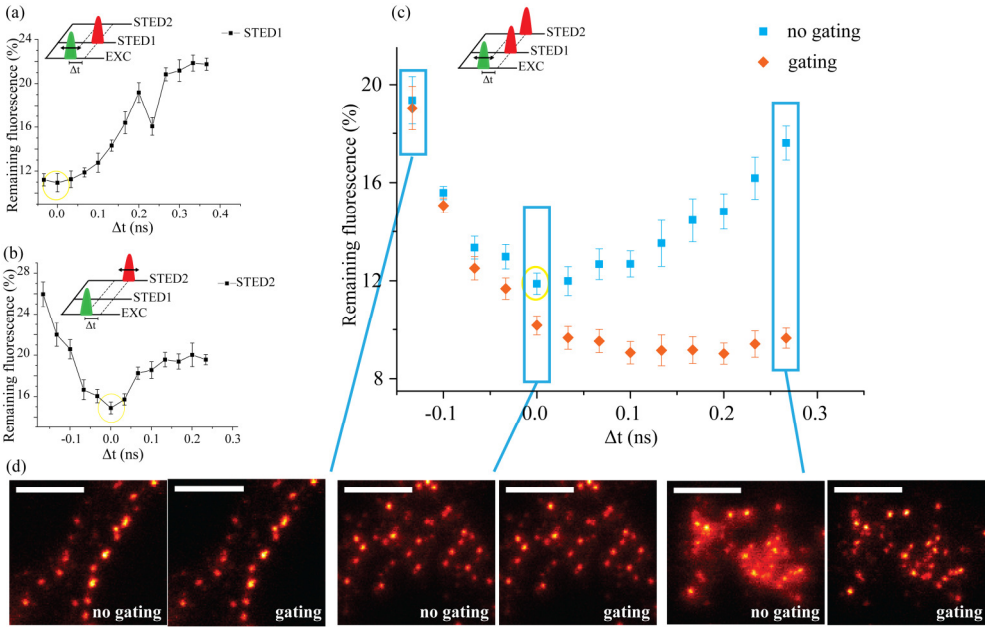

Fig. 3. STED inhibition as function of the time delay between the excitation beam and the STED beams (a,b,c) (mean ± s.d; n = 10) . The inhibition is estimated respectively for the first STED beam acting solely (a), the second STED beam acting solely (b) and the two beams acting simultaneously (c). The yellow circles depict the position obtaining the highest depletion effect. In the case of time gated detection, inhibition is obtained by collecting the fluorescence immediately after the STED beams action. The inserted time-scale of the pulses are symbolic and not to scale. Comparison between STED and g-STED imaging of synaptic vesicles for different time delay between the excitation and the STED pulses (d). Excitation 572/15 nm, Detection 641/75 nm, Depletion 720/20 nm. Excitation average power ~4 µW (a-c) and ~0.6 µW (d); STED1 average power ~970 µW (a- c) and ~1.1 mW (d); STED2 average power ~970 µW. The scale bars in these images are 1 µm.

Even though the relative residual fluorescence increases for later depletion, time-gated detection can compensate this misalignment: in the case of late depletion ($\Delta t > 0$), the

#161451 - $15.00 USD Received 13 Jan 2012; revised 26 Feb 2012; accepted 1 Mar 2012; published 15 Mar 2012

efficiency of quenching does not deteriorate if the fluorescence signal is collected after the STED action. Obviously, time-gated detection cannot compensate for early depletion ($\Delta t < 0$). We confirmed the effects of time-gated detection by imaging synaptic vesicles immunolabeled with same dye molecule, i.e. ATTO 594 (Fig. 3(d)). As the pulse width of the STED beams (~80 ps) is much shorter than the excited state lifetime of the fluorophores labeling the cell structures (~3 ns), when the system was well aligned in time, the effect of time-gated detection was negligible (Fig. 3(d), left panel). On the other hand, the contrast of STED imaging reduced for late depletion, but it was completely recovered by applying time-gated detection (Fig. 3(d), middle and right panels). However, time-gated detection reduces the peak brightness, and thereby the signal-to-noise/background ratio (SNR and SBR) of the images, particularly when it has to compensate for very late depletion [23]. Thereby, for application limited by the SNR or the SRB time-gated detection cannot be used and an accurate temporal alignment of the excitation and STED beam is mandatory. Interesting, for STED architecture based on different source for STED and excitation beam synchronization jittering can preclude an accurate alignment, in such a case time-gated detection offer an important solution.

4.2 Polarization state of STED beams

In this section we work on the optimization of the "zero"-intensity point of the doughnut foci (named γ in section 3 and Fig. (2)). In our STED microscope, two vortex phase plates are used for creating the doughnut of each STED beam, which is rather tolerant to many experimental imperfections such as astigmatic or spherical wave front aberrations or lateral misalignments [31]. Using a vortex phase plate, an imperfect "zero" typically stems from wrongly polarized light [27, 32]. In particular, the center of the doughnut PSF is practically zero when the STED beam is circularly polarized with the appropriate circular orientation. For optimizing the polarization, a combination of a half-wave plate and a quarter-wave plate was used to achieve circular polarization at the back-aperture of the objective lens. So far, we focused on the performance of the microscope by misaligning the polarization state of the STED beam in a controlled way. Therefore, we used only one STED beam (STED1) and rotated the quarter-wave plate while keeping the position of the half-wave plate constant, to achieve non-circular polarization states. In order to quantify the performance fall of the setup, we imaged single fluorescent beads and compared the peak brightness in the STED image relative to the confocal counterpart. Figure 4(a) shows the remaining peak intensity for various polarization states of the STED beam. Slight deviations from the circular polarization induce substantial reductions of the relative peak brightness. Notably, with a circular polarization, but in the wrong orientation, imaging is nearly impossible, since the remaining peak brightness falls down to well below 20% of the confocal counterpart. This limitation is fully confirmed by imaging of biological sample (Fig. 4(b)). When the STED beam is circularly polarized the resolution improvement is evident comparing STED and confocal images. On the other hand the resolution improvement can be hidden by noise and background when the polarization status of the STED discards from the optimal position.

#161451 - $15.00 USD Received 13 Jan 2012; revised 26 Feb 2012; accepted 1 Mar 2012; published 15 Mar 2012

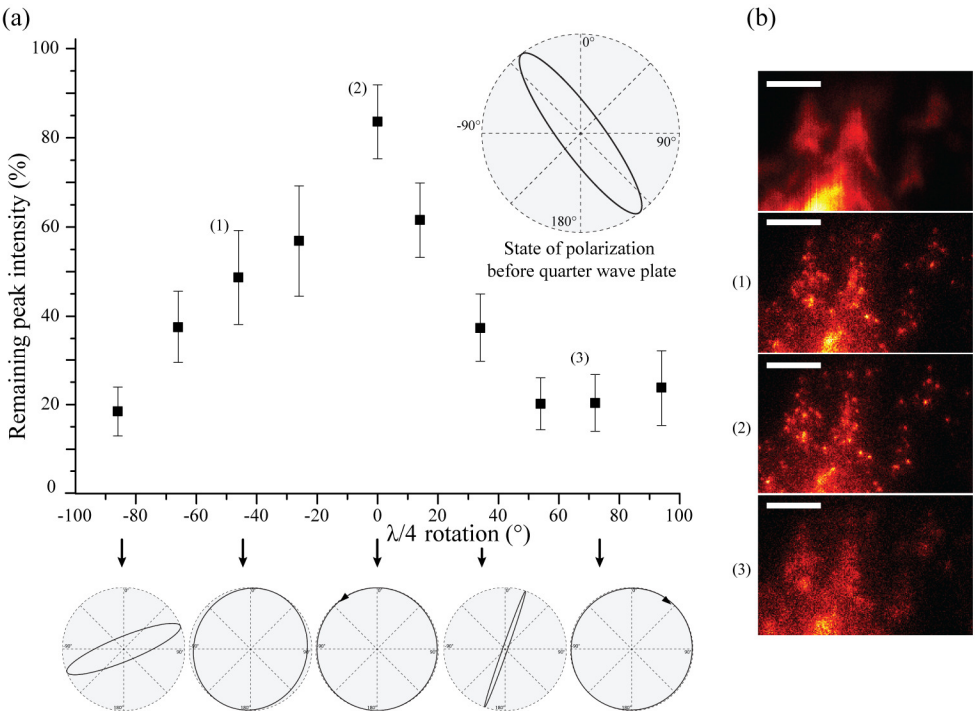

Fig. 4. (a) Remaining peak intensities between confocal and STED imaging for single isolated fluorescent beads as function of the STED beam polarization (mean ± s.e.m; n = 12). For each state of polarization we acquired three images: one in confocal modality, one in STED modality and the last again in confocal modality. We used the two confocal images to take into account the possible bleaching occurring during the imaging. (b) Comparison of synaptic vesicles imaging between confocal (upper panel) and STED with three different states of polarization. Excitation 572/15 nm, Detection 641/75 nm, Depletion 720/20 nm. Excitation average power ~4 μW (a) ~0.2 μW (b); STED average power ~970 μW (a) and ~1.1 mW .

4.3 STED Imaging

To gain highest resolution in our STED microscope we use both STED beams in parallel for fluorescence imaging of calibration and biological samples. Surely, by the use of two beams any imperfections in terms of the parameters δ and γ as discussed before would influence the final PSF even more significant. Accordingly, after we performed optimization steps highlighted in the previous sections, we addressed super-resolution imaging. We first compared confocal and STED images of 40 nm red fluorescent beads (Fig. 5(a) and 5(b)). This comparison clearly shows the substantial resolution enhancement obtained by means of STED microscopy. Line profiles across typical images of single beads displayed a full-width at half-maximum (FWHM) of 54.0 ± 0.8 nm (mean ± s.d.; n = 23) when exploring simultaneously the full power of the two STED beams, i.e. 14 mW. Considering the 40 nm diameter size of the beads, this implies an optical resolution ~46 nm in the focal plane.

Additionally, we used our setup to image the distribution of synaptic vesicles in nerve terminals of hippocampal neurons (Fig. 5(f) and 5(g)). Synaptic vesicles are intracellular organelles of 40-50 nm in diameter that contain neurotransmitters and undergo intense trafficking synchronized with the electrical activity of the neuron [33]. By comparing the confocal with the respective STED image, we show the strong resolution improvement that we can achieve on a biological sample. STED imaging discloses morphometric properties that are completely hidden to the confocal observation.

#161451 - $15.00 USD Received 13 Jan 2012; revised 26 Feb 2012; accepted 1 Mar 2012; published 15 Mar 2012

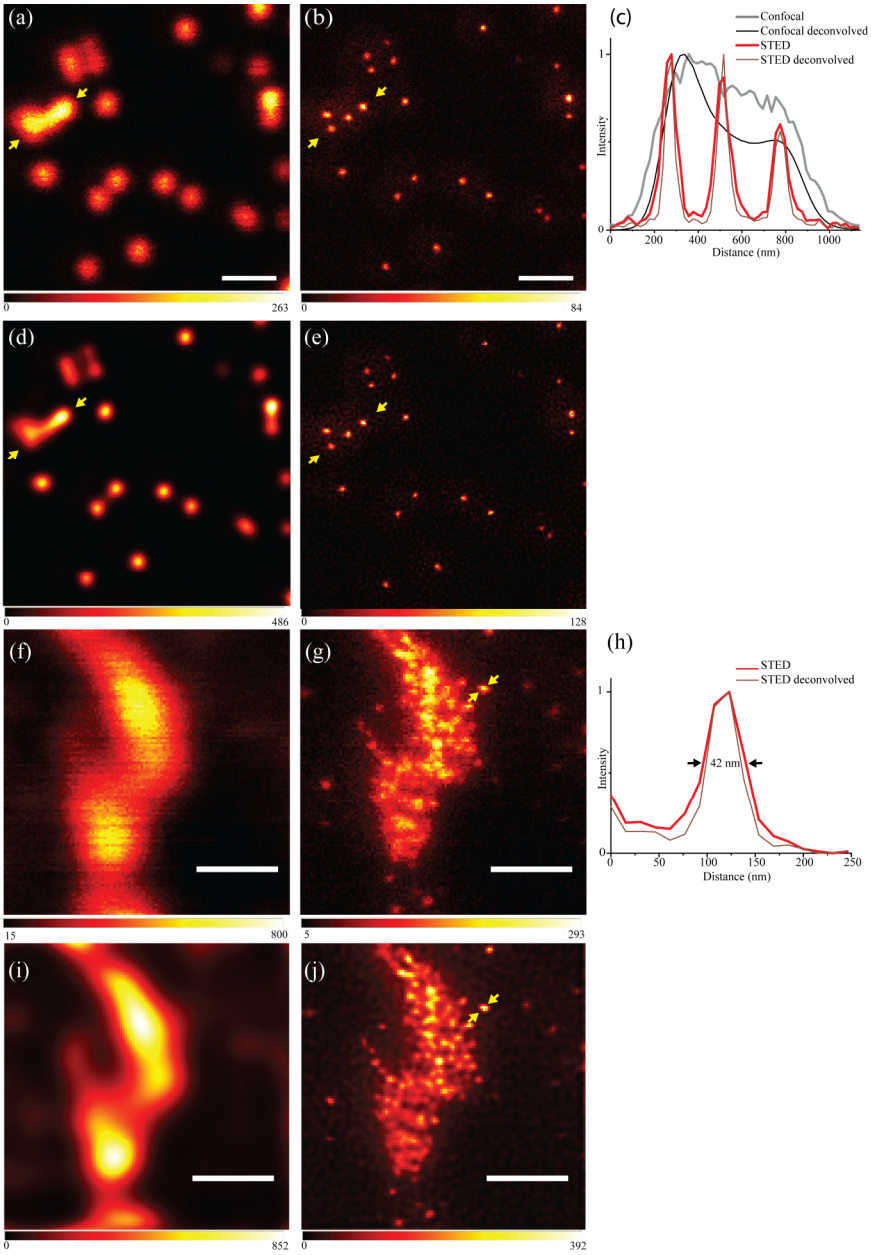

Fig. 5. Resolution enhancement with STED microscopy. Fluorescent beads imaged in standard confocal mode (a), high-resolution STED (b) and the corresponding deconvolved ones (d, e). The plot (c) shows a confocal (grey), STED (red), confocal + deconvolution (thin black) and STED + deconvolution (thin dark red) line profiles along the arrows indicated in the images. Synaptic vesicles in GABAergic terminals of hippocampal neurons labeled with VGAT observed in standard confocal mode (f). In contrast, STED (g) reveals details of single vesicles which are unobservable in the confocal image. Both images show raw data. (i) and (j) show the corresponding deconvolved images. (h) Profile along the line indicated by arrows in the STED image reveals a resolution around 40 nm (red), corresponding to the average size of individual synaptic vesicles. For comparison we show also the corresponding profile of the deconvolved image (thin dark red). Excitation 572/15 nm, Detection 641/75 nm, Depletion 720/20 nm. Pixel size 15 nm. Excitation average power ~4 µW; STED average power ~4.2 mW. Scale bar of 0.5 µm. (d), (e), (i) and (j) are obtained after 10 iterations of a Richardoson-Lucy based deconvolution algorithm regularized by a moderate quadratic potential term.

#161451 - $15.00 USD Received 13 Jan 2012; revised 26 Feb 2012; accepted 1 Mar 2012; published 15 Mar 2012

The apparent size of non-specifically bound single subresolved antibodies indicates a lateral resolution of the STED microscope down to 42 ± 2.4 nm (mean ± s.d.; n = 12). It is worth noting that this value is in good agreement with the resolution estimated by measuring single isolated fluorescent beads. The slight differences in resolution obtained between imaging of fluorescent beads and single antibody is not surprising, despite the identical imaging conditions have been used, i.e. power and wavelength of STED beams. In fact, the fluorophores that fill the beads and ATTO590 fluorophores used in the biological sample may differ for stimulated emission cross-section and thereby quenching efficiency.

It is worth noting that the images of Fig. 5 (a), 5(b), 5(f) and 5(g) are raw data; nevertheless we performed further deconvolution based on Richardson-Lucy algorithm (Fig. 5(d), 5(e), 5(i) and 5(j)) [34]. The deconvolved images confirm the significant resolution improvement by STED over to confocal. Although the contrast is increased no relevant further information is added at the images.

5. Discussion and conclusion

In this work, we mainly focused on some experimental keypoints in a homemade STED microscope to gain the highest performances. The setup used for the experiments is based on a single white light supercontinuum laser source producing the excitation and depletion beams. Special attention has to be taken for the temporal alignment of the STED and excitation beams. Nevertheless, time-gated detection offers a nice trick to compensate temporal misalignment, noise and background can preclude its implementation. On the other side, time-gated detection can be particularly useful to compensate synchronization jittering in the STED architecture where STED and excitation beams are delivered by different sources.

In simulation and experiment we showed the influence of an imperfect zero intensity point in the center of the STED doughnut and we demonstrated that the polarization is the most prominent factor influencing the zero intensity point. Finally after going through the optimization steps, we were able to gain highest resolution of our STED microscope and we presented images in calibration and biological samples in which the STED resolution can be numbered well below 45nm.

Although we presented only results based on a SC setup, time alignment optimization is extremely important for any pulsed STED architecture, thereby including stimulated-Raman-scattering [35] and mode-locked based laser sources. On the other hand, polarization status optimization is crucial for any vortex based STED setup including CW-STED, where temporal alignment is not needed.

We claim that the optimization of the highlighted keypoints can significantly increase the performance of any STED microscope and make the design and the alignment of such optical setup more convenient and straightforward.

Acknowledgments

We thank Andrea Raimondi (Neuroscience and Brain Technologies, Istituto Italiano di Tecnologia, Genoa, Italy) for the precious help in the preparation of the biological specimens.

#161451 - $15.00 USD Received 13 Jan 2012; revised 26 Feb 2012; accepted 1 Mar 2012; published 15 Mar 2012